GDCh Research Article Angewandte International Edition Chemie www.angewandte.org

How to cite: *Angew. Chem. Int. Ed.* **2025**, *64*, e202508512
doi.org/10.1002/anie.202508512

Photocatalysis

An Atomically Dispersed Photocatalyst for Undirected *para*-Selective C–H Bond Functionalizations

*Suman Pradhan[+], Jun Hu[+], Peng Ren, Yuman Qin, Noopur Jain, Susanna Monti, Giovanni Barcaro, Aleksander Jaworski, Xingchao Dai, Jabor Rabeah, Joaquin Silvestre-Albero, Veronica Celorrio, Anna Rokicińska, Piotr Kustrowski, Sandra Van Aert, Sara Bals, and Shoubhik Das**

Abstract: Regioselective C–H bond functionalization is pivotal in modern scientific exploration, offering solutions for achieving novel synthetic methodologies and pharmaceutical development. In this aspect, achieving exceptional regioselective functionalization, like *para*-selective products in electron-poor aromatics, diverges from traditional methods. Leveraging the advantages of atomically dispersed photocatalysts, we designed a robust photocatalyst for an unconventional regioselective aromatic C–H bond functionalization. This innovation enabled *para*-selective trifluoromethylations of electron-deficient metadirecting aromatics (–NO_2, –CF_3, –CN, etc.), which is entirely orthogonal to the traditional approaches. Mechanistic experiments and DFT analysis confirmed the interaction between Cu-atom and the aromatic substrate, alongside the photocatalyst's molecular arrangement, driving selective exposure of the *para*-selective functionalization. This strategic approach elucidated pathways for precise molecular transformations, advancing the frontier of regioselective C–H bond functionalization by using atomically dispersed photocatalysts in organic synthesis.

Introduction

The regioselective aromatic C–H bond functionalization has become a viable approach for intricate molecular targets due to their high atom efficiency and development of sustainable chemistry.[1] Nevertheless, the precise functionalization of the aromatic C–H bond continues to pose a challenge due to the subtle differences in reactivity among the multiple C–H bonds present within the substrate.[2] Heading down this path, the noteworthy electrophilic aromatic substitution, also recognized as the Friedel–Crafts (FC) reaction (Figure 1a),[3] finds extensive utility. According to the traditional FC reactions, electron-rich aromatic compounds yield products in a nearly equimolar mixture of *ortho/para*-selectivity and electron-deficient aromatics generate primarily *meta*selective products upon encountering electrophilic species. These reactions are both influenced by the electron-density aspect, which is contingent upon the specific substituents within the

[*] Dr. S. Pradhan[+], J. Hu[+], Dr. P. Ren, Dr. Y. Qin, Dr. S. Das
Department of Chemistry, University of Bayreuth Universitätsstraße 30 95447, Bayreuth, Germany
E-mail: Shoubhik.Das@uni-bayreuth.de

Dr. S. Pradhan[+], J. Hu[+], Dr. P. Ren, Dr. Y. Qin, Dr. S. Das
Department of Chemistry, University of Antwerp, Antwerp 2020, Belgium

Dr. N. Jain, Dr. S. Van Aert, Dr. S. Bals
EMAT and NANOlab Center of Excellence, Department of Physics, University of Antwerp, Antwerp 2020, Belgium

Dr. S. Monti
CNR-ICCOM Institute of Chemistry of Organometallic Compounds, Pisa 56124, Italy

Dr. G. Barcaro
CNR-IPCF Institute for Chemical and Physical Processes, Pisa 56124, Italy

Dr. A. Jaworski
Department of Materials and Environmental Chemistry, Stockholm University, Stockholm 10691, Sweden

X. Dai, Dr. J. Rabeah
Leibniz-Institut für Katalyse e. V, Albert-Einstein-Straße 29a 18059, Rostock, Germany

Dr. J. Rabeah
State Key Laboratory of Low Carbon Catalysis and Carbon Dioxide Utilization, Lanzhou Institute of Chemical Physics (LICP), Chinese Academy of Sciences, Lanzhou 730000, P.R. China

Dr. J. Silvestre-Albero
Departamento de Química Inorgánica, Instituto Universitario de Materiales, Universidad de Alicante, Alicante E-03080, Spain

Dr. V. Celorrio
Diamond Light Source Ltd, Oxfordshire, Didcot OX11 0DE, UK

Dr. A. Rokicińska, P. Kustrowski
Faculty of Chemistry, Jagiellonian University, Gronostajowa 2, Kraków 30–387, Poland

[+] Both authors contributed equally to this work.

Additional supporting information can be found online in the Supporting Information section

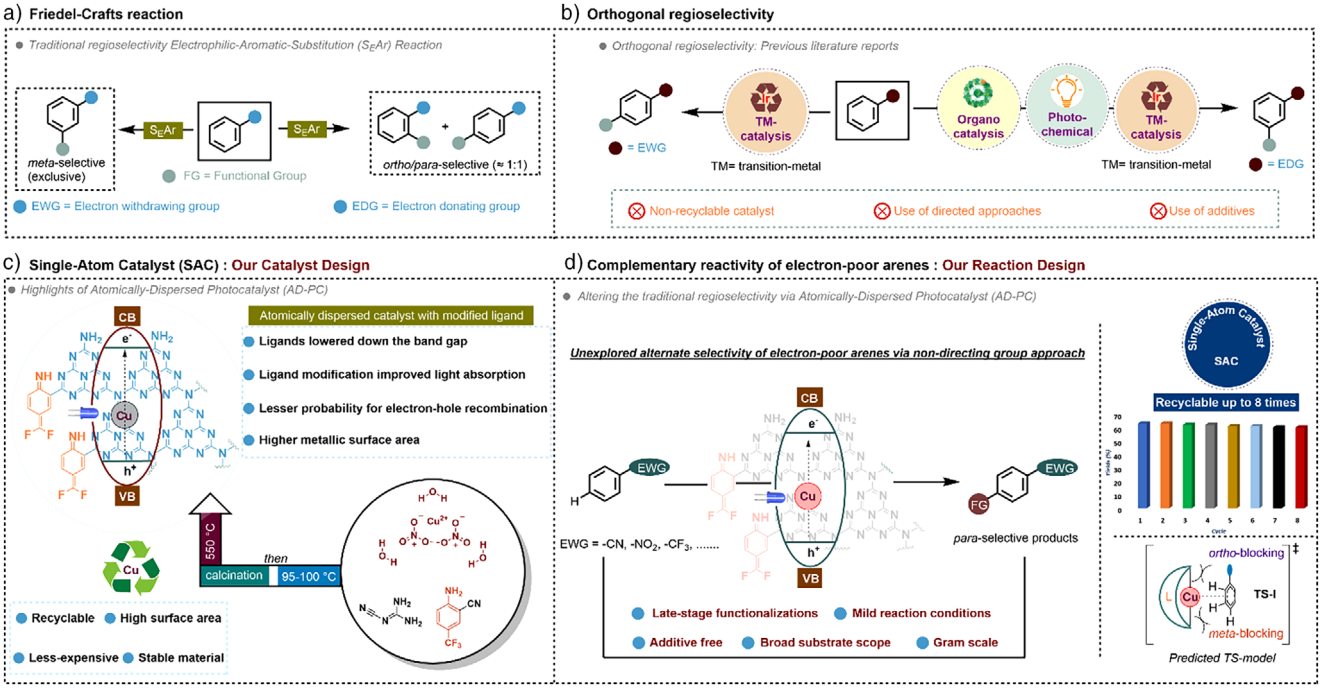

Figure 1. Aromatic C—H bond functionalization: state-of-the-art and our model of work.

molecule. Therefore, the challenge lies in altering the regioselectivity pattern, explicitly focusing on *para*-C—H bond functionalization of electron-poor arenes and *meta*-C—H bond functionalization of electron-rich arenes. To address this challenge, contemporary chemists have explored this captivating field, developing photocatalytic methods[4] and transition-metal catalytic techniques[5] to achieve *meta*selective C—H bond functionalization in electron-rich arenes (Figure 1b).[6] Recent studies have strategically employed *N*-heterocyclic carbenes (NHCs) in photocatalysis and L-shaped ligands in transition-metal catalysis to introduce steric hindrance at the ortho and para positions, thereby promoting metaselectivity. However, these approaches are limited using nonrecyclable catalysts, the need for stoichiometric additives, and the complexity of multistep reaction sequences, all of which pose challenges to their broader applicability and sustainability. On the other hand, *para*-selective functionalization is also established, however, regioselectivity has predominantly been governed by the electron-rich directing groups, bulky catalysts or formulating ligands with a templating effect in the presence of homogeneous catalysis (Figure 1b).[7–15] The reliance on nonrecyclable catalysts raises sustainability concerns,[16,17] along with the need for preinstalled directing groups such as ketones, esters, or amides for electron-poor arenes.[18–20] Additionally, the use of stoichiometric Lewis acids and the involvement of multistep reactions complicate the synthetic processes, often leading to increased costs and reduced efficiency in the overall reaction scheme. Hence, achieving *para*-selective functionalization of electron-deficient arenes following an undirecting strategy, remains a challenge in organic synthesis which is yet to overcome.[12,21]

In this context, designing single metal atom catalysts (SACs) for regioselective functionalization is highly effective due to their unique reactivity and reusability, bridging the gap between heterogeneous and homogeneous catalysis (Figure 1c). This type of catalyst offers the highest atom utilization efficiency, and thanks to advanced characterizations techniques, the structure–activity relationships of the active sites can also be elucidated. The support materials onto which transition metal atoms are deposited in SAC play a crucial role by facilitating charge transfer and enhancing photocatalytic reactivity.[22] In this aspect, polymeric carbon nitrides (PCN), as a support material, have recently become an invaluable support to design robust SACs due to their exceptional stability, high surface area, and tunable chemical properties, ultimately enhancing their catalytic activity, and enabling precise control over their reactivity.[23–26] Importantly, from a sustainability perspective, nitrogen–substituted carbon framework and PCN emerge as promising green photocatalysts due to their reliance on abundant elements during the design and preparation phases.[27,28] Considering this, tremendous efforts have been made to achieve transformations such as small molecule activations.[22–28] However, their application into regioselective C—H bond functionalization is still in its infancy. To address this gap, an atomically dispersed Cu-photocatalyst has been designed by adding copper to a nanocrystalline PCN support with approximately 2 Å distance. We have specifically functionalized the parent g-C_3N_4 core by including aryl amino moiety to reduce the band gap, hence enhancing light absorption, and doped it with low-toxic, earth-abundant Cu metal to mitigate electron-hole charge recombination. With the photocatalyst design, our objective was to realize a *para*-selective aromatic C—H

bond trifluoromethylation since the inclusion of a trifluoromethyl (—CF_3) group within a molecule imparts heightened pharmacokinetic attributes, encompassing enhancements in metabolic stability, permeability, and affinities for protein binding.[29] Compounds containing a trifluoromethyl group (—CF_3), particularly aromatic and heteroaromatic molecules, are frequently encountered in diverse domains such as drugs, agrochemicals, organic dyes, and polymers.[30] Therefore, the introduction of this motif and its unique characteristics highlights the achievements of chemical synthesis, especially given its notable absence in nature.

Our hypothesis for achieving this high regioselectivity involved the use of an atomically dispersed Cu on aryl-amino-functionalized graphitic carbon nitride (Cu@f-gC_3N_4, f = functionalized) photocatalyst, which plays a crucial role in a regio-determining step by interacting with the aromatic substrate in a η^2 fashion. Sterically hindering the *ortho*- and *meta*-positions (Figure 1d, TS–I) enables the alternate regioselective functionalization of aromatic C—H bonds in electron-poor aromatic compounds. A thorough examination of the structure and mechanisms confirms the cooperative behavior of metal centers in neighbouring sites, facilitating the efficient activation of substrates through a dynamic bridge-coupling mechanism.

Results and Discussion

In this study, nitrobenzene(**1a**) was functionalized at *para*-position with Togni-I's reagent (**2a**) ($E_{1/2} = -0.45$ V vs. SCE in MeCN) as the trifluoromethylating reagent and Cu@f-gC_3N_4 (5 mg, with a Cu loading of 0.2 wt%, w.r.t. metal precursor which corresponds to 0.045 µmol of Cu) as the photocatalyst in MeCN. Nitrobenzene was selected as the model substrate due to the electron-withdrawing nature of the nitro group, which depletes electron density on the aromatic ring through both inductive and resonance effects. The band gap of Cu@f-gC_3N_4 was determined to be 2.65 eV from the Tauc plot. Mott–Schottky analysis revealed a conduction band potential (E_{CB}) of —1.40 V (vs. SCE in MeCN) and a valence band potential (E_{VB}) of +1.25 V (vs. SCE in MeCN), making it suitable for the reduction of the Togni-I reagent.

The reaction mixture was irradiated under 390 nm Kessil lamp for 3 h by maintaining the reaction temperature to 30 °C. To our delight, the desired *para*-selective product (**3a**) was isolated in 67% yield with a *p/m* ratio of 8:1 (Table 1, entry **1**). Alternative, commonly available solvents such as DCE, DMF, DMSO, EtOH, and HFIP proved to be unfavorable in terms of both yield and the selectivity ratio (Table 1, entries **2–6**). In an endeavor to enhance the *p/m* ratio, different light sources with varying wavelengths (427 and 456 nm Kessil lamps) were explored and led to yields of 65% and 61%, respectively, with a *p/m* ratio of 10:1 (Table 1, entries **7–8**). This investigation motivated the adoption of a lower-energy light source (a blue LED strip) for the transformation and in fact, with the utilization of this LED strip, the targeted product **3a** was obtained with a yield of 60% and 64% with a 10:1 *p/m* ratio in 3 and 6 h, respectively. (Table 1, entries **9–10**). The selection of a blue LED is also supported by the UV–vis DRS and Mott–Schottky measurements. Our hypothesis suggested that the selectivity of this transformation was mainly driven by the interaction between the metal catalyst and the substrate. When using high-energy light sources, the intermediate tends to break apart easily, leading to less selective outcomes. In contrast, the lower energy from blue LEDs helped to maintain the integrity of the intermediate, making it more suitable for our reaction and enhancing selectivity. After the allotted reaction time, approximately 70% of the starting aromatic compounds had reacted, suggesting their relatively low reactivity. Meanwhile, the excess trifluoromethylating reagent began to decompose into a known side product (S2.9, Supporting Information). Extending the reaction time further did not improve the yields or the conversion rate. The use of other trifluoromethylating reagents such as CF_3SO_2Cl, Togni-II, and Umemoto's reagent did not also provide satisfying results (Table 1, entries **11–13**). Notably, in the absence of light, no product was formed, unequivocally affirming the pivotal role of photons in this reaction (Table 1, entry **14**). Only 10% of the desired product was obtained when the photocatalyst was omitted from the reaction (Table 1, entry **15**). Thus, the background reaction occurs but was inefficient and unselective. Furthermore, we have performed a large-scale reaction with 25 mmol of **1a** (3 g, see S2.5) and this scale-up reaction yielded 52% of the product by maintaining a 10:1 *p/m* ratio. Additionally, to assess the stability of the photocatalyst, a photocatalytic trifluoromethylation reaction of nitrobenzene (**1a**) with Togni-I (**2a**) was recycled for at least seven consecutive cycles under the identical reaction

Table 1: Optimization of reaction conditions.

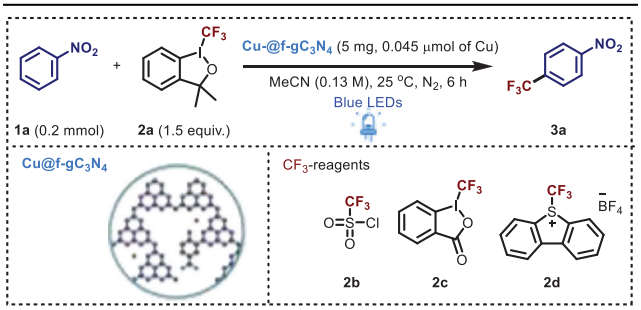

Entry	Reaction conditions	Yields (%)	Ratio (p/m)
1	MeCN, 390 nm Kessil, and 3 h	67	8/1
2	DCE, 390 nm Kessil, and 3 h	50	7/1
3	EtOH, 390 nm Kessil, and 3 h	5	3/1
4	HFIP, 390 nm Kessil, and 3 h	25	3/1
5	DMF, 390 nm Kessil, and 3 h	40	5/1
6	DMSO, 390 nm Kessil, and 3 h	42	5/1
7	MeCN, 427 nm Kessil, and 3 h	65	10/1
8	MeCN, 456 nm Kessil, and 3 h	61	10/1
9	MeCN, blue LEDs, and 3 h	60	10/1
10	MeCN, blue LEDs, and 6 h	64	10/1
11	CF_3SO_2Cl (**2b**)	52	7/1
12	Togni-II (**2c**)	59	10/1
13	Umemoto's reagent (**2d**)	66	7/1
14	no light	0	
15	no catalyst	10	1/10
16	f-gC3N4	25	3/1

conditions (Figures 1c, S2.4, ESI). The high reproducibility of the yield across multiple recycling experiments highlights the excellent stability and photocatalytic efficiency of the Cu@f-gC_3N_4 catalyst. In contrast, when the Cu-free support (f-gC_3N_4) was used under identical conditions, both the yield and regioselectivity dropped significantly-from 64% yield and a 10:1 para-to-meta ratio to 25% yield and a 3:1 ratio (Table 1, entry 16). These results clearly indicate that the presence of Cu is essential for achieving high catalytic efficiency and *para*-selectivity. Importantly, Cu alone does not confer this effect; rather, it is the synergistic interaction between the isolated Cu atoms and the f-gC_3N_4 support that governs both the reactivity and the regioselectivity of the transformation (see S2.6 in Supporting Information for detailed comparison). After optimizing the reaction conditions, the kinetics of this reaction were also investigated and revealed the steady linear increase of the yield while keeping the *p/m* ratio of the product always constant (S2.7, Supporting Information).

After optimizing the reaction conditions (Table 1, entry **10**), the scope of this reaction was investigated by applying it to different aromatic compounds (Figure 2a). Initially, in alignment with our hypothesis, commonly recognized electron-deficient aromatic compounds such as trifluoro- and cyano-benzene were examined and yielded a *para*-selective product up to the yield of 50%–44% with a selectivity ratio of 5:1–4:1(**3b-c**). In addition to derivatives of trifluoro- and cyano-benzene, other electron-poor arenes such as azobenzene, 4-methoxy azobenzene, and phenylsulfoxide also produced their respective products with satisfactory yield and selectivity (**3d–f**). The obtained results revealed that the efficacy of electron-withdrawing groups may be attributed to the plausible interaction between polar groups present in the substrate and the photocatalyst throughout the course of the reaction. These interactions played a pivotal role in influencing the overall reaction pathway, thereby serving as critical factors for comprehending the mechanistic intricacies inherent in the photochemical process. Further introduction of various substitutions at different positions on the aromatic ring of electron-poor arenes, including -halide and -alkyl groups, did not compromise the yield and selectivity (**3g–m**). The additional substituents are positioned in regions that do not interfere with the η^2-binding mode. DFT analysis (Figure S8, Supporting Information) shows that substituents orient away from the Cu-ligand interface, minimizing steric interference. Substituted electron-deficient arenes, particularly those containing nitro groups, exhibited favorable reactivity, underscoring the consistent engagement of these substituents in interaction phenomena with the photocatalyst.

To demonstrate the broad applicability of this photocatalytic system, we tested other hypervalent iodine compounds as radical precursors for the regioselective functionalization of electron-poor arenes beyond just $-CF_3$ derivatives (Figure 2b). To our delight, halogenation (−F and −Cl) of electron-poor arenes also went smoothly, yielding product **3n–q** in moderate to good yields with modest regioselectivity.In addition to its effective application to electron-deficient aromatic compounds, this approach has been successfully extended to electron-rich molecules (Figure 2c). In this regard, it is worth noting that the regioselective trifluoromethylation of electron-rich arenes was previously attained by several research groups by using homogeneous photoredox catalysis,[30] transition-metal catalysis,[31] or electrochemical processes.[32] However, these methods suffer from the use of nonrecyclable photocatalysts, prefunctionalized arene, and stoichiometric use of additives. Following our reaction conditions, a variety of anisole derivatives produced *para*-selective trifluoromethylated products with exceptional selectivity (**3r–s**). Unlike traditional electrophilic aromatic substitution reactions that yield a mixture of *ortho* and *para* products, our designed photocatalyst afforded specifically *para*-selective products under these reaction conditions. Small molecules such as phenol, fluorobenzene, and iodobenzene also produced trifluoromethylated products with high selectivity (**3t–v**). Although our devised reaction conditions facilitated the smooth generation of corresponding products from oxygenated, halogenated, and alkylated arenes, chlorobenzene exhibited sluggish reactivity under the reaction conditions, attributable to the higher electron affinity of chlorine relative to fluorine and iodine.

Furthermore, electronically neutral molecules such as benzene, isopropyl, and *tert*-butyl benzene demonstrated robust reactivity under our reaction conditions, yielding the corresponding products up to the yields of 50%–52% and selectivity of 10:1 (**3w–y**). To our observation, different protected and unprotected *N*-alkyl anilines (**3z-ad**), afforded a series of aryl trifluoromethylated products in good to excellent yields (53%–83%), maintaining the high regioselectivity (up to 20:1). A notable observation was made when heterocyclic ring with an aromatic amine was employed, selective trifluoromethylation occurred at the C-2 position of the thiophene moiety, driven by the elevated electron richness of the heterocycle (**3ae;** 56%). Additionally, while conducting the reaction of mixing both nitrobenzene and a toluene derivative under our standard conditions the yields of compounds **3a** and **3x** were 28% and 31%, respectively, which excludes Hammett type LFER phenomena.

Encouraged by these promising results, we explored the application of this photocatalyst in late-stage transformations (LST), an effective strategy for precise chemical modifications in complex molecules. Notably, LST enables the functionalization of complex molecular structures, yielding novel and valuable compounds.[33] Recognizing the potential of aromatic CF_3-containing molecules to enhance antibiotic, antitumor, and antidepressant properties in pharmaceuticals, we reasoned that our straightforward synthetic approach should pave the way for advancing drug discovery through LST. As shown in Figure 2d, the (+)-dehydroabietylamine was effectively functionalized to **3af** in 67% yield, which might become an interesting candidate for fragrance and triple-negative breast cancer treatment. Furthermore, a trifluoromethyl group was successfully installed in a fungicide (famoxadone) to protect agricultural products against various fungal diseases on fruiting vegetables (**3ag**, 51%). In addition to LST, we have pursued the direct synthesis of pharmaceutical compounds from their immediate precursors. The antidepressant fluoxetine (**3ah**), a selective serotonin reuptake inhibitor with affinities for various serotonin receptors, was successfully synthesized through our approach.

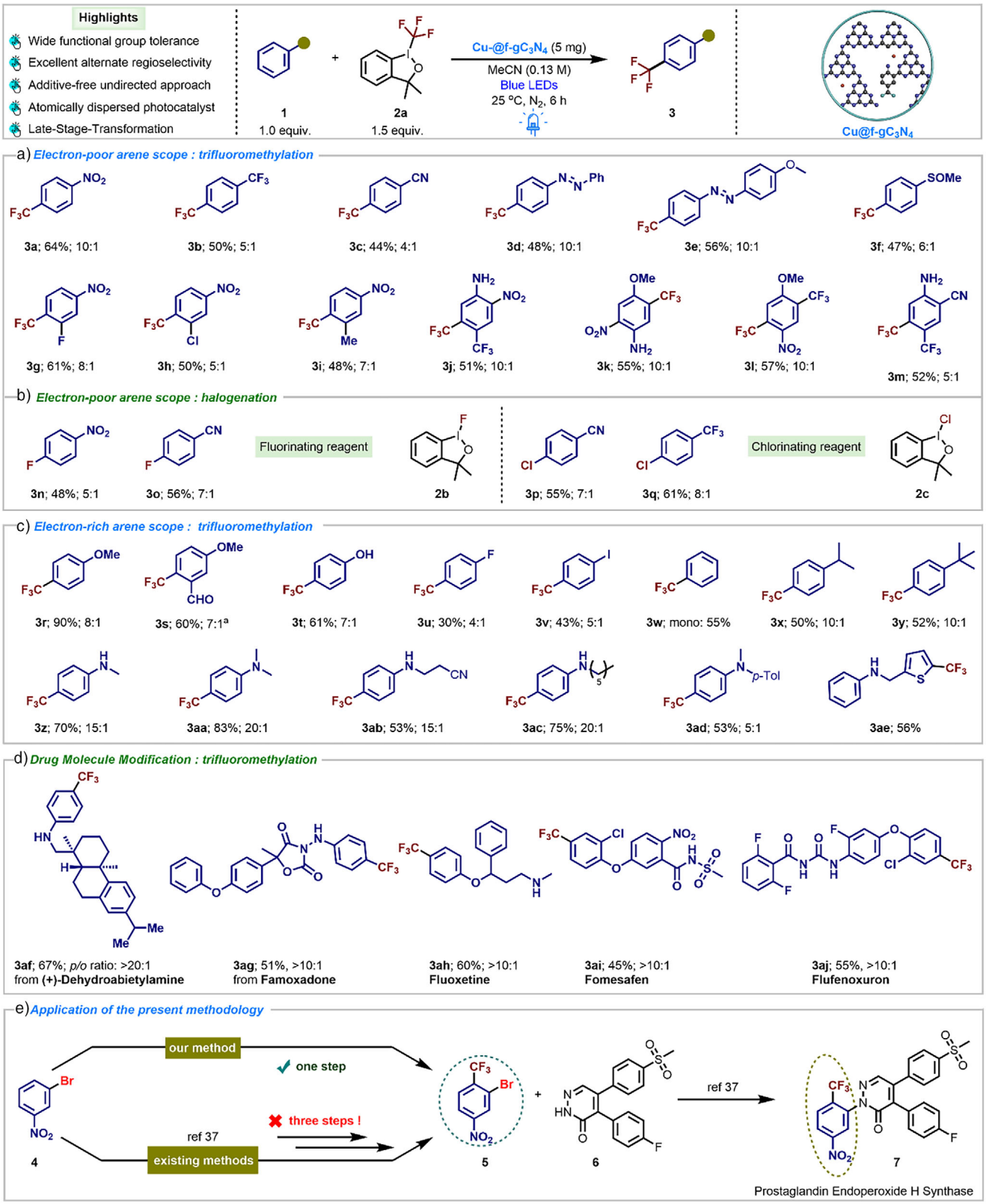

Figure 2. Trifluoromethylation substrate scope. Reaction conditions: **1** (0.2 mmol, 1 equiv), **2a** (0.3 mmol, 1.5 equiv), catalyst (5 mg), MeCN (0.13 M) irradiated under blue LED irradiation for indicated time at room temperature. [a]CF_3SO_2Cl (**2b**) was used instead of **2a**. The ratio mentioned is *p/m* in Figure 2a,b and *p/o* Figure 2c,d.

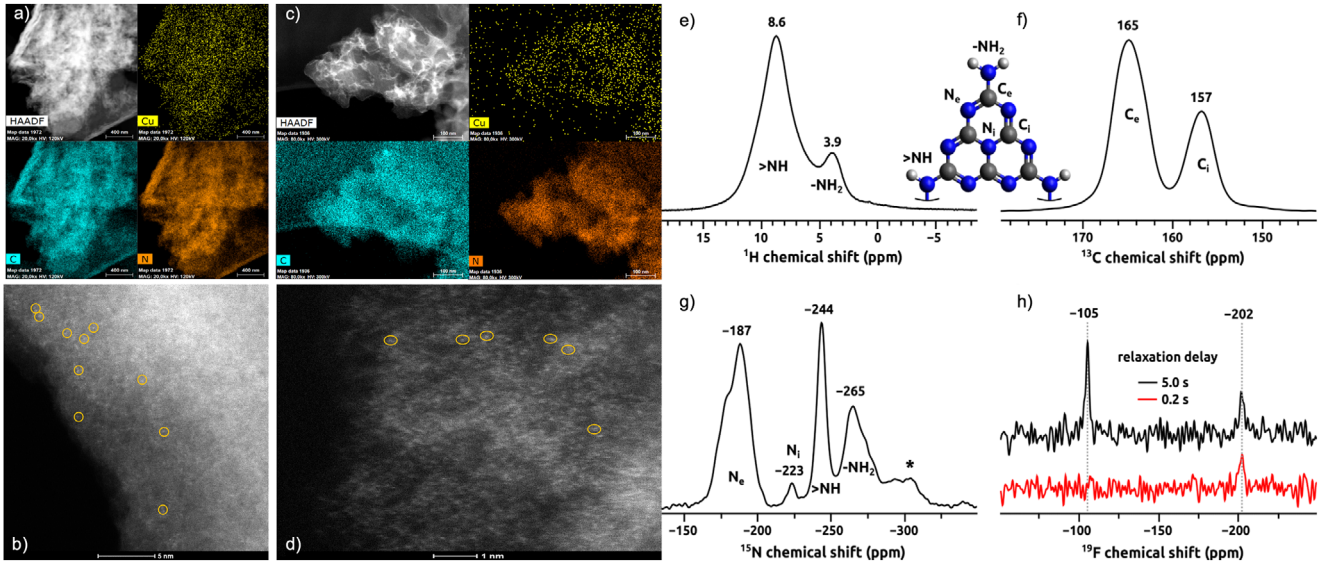

Figure 3. HAADF–STEM image and EDX mapping and solid-state NMR: a), b) HAADF–STEM EDX elemental maps (scale bar: a) 400 nm and c) 100 nm) and a high-resolution image of the fresh catalyst and c), d) the catalyst after reaction respectively. e) ^{1}H MAS, f) ^{1}H—^{13}C CPMAS, g) ^{1}H—^{15}N CPMAS, and h) ^{19}F MAS NMR spectra of Cu@f-gC_3N_4 catalyst at 14.1 T. Spinning sideband is marked with an asterisk.

Employing *N*-methyl-3-phenoxy-3-phenylpropan-1-amine as the precursor yielded the drug molecule with a significant yield and selectivity (60%, 10:1). This subtle structural modification led to a remarkable enhancement in serotonin uptake selectivity.[34] Additionally, the diphenyl ether derivative, fomesafen (**3ai**), was synthesized from its direct precursors with a moderate yield but notable *para*-selectivity (45%, 10:1). This transformation resulted in the production of one of the most widely used herbicides in soybean and peanut fields, owing to its potent herbicidal activity at low concentrations.[35] The synthesis of flufenoxuron (**3aj**) using our approach yielded the desired product with a 55% yield. This trifluoromethylated product, recognized as a benzoylurea pesticide, serves as an insect growth regulator and chitin synthesis inhibitor, effectively controlling immature stages of insects.[36] Our proposed methodology can also be applied to synthesize several important biologically active molecules containing a *para*-CF_3 group on an electron-poor arene as a key structural motif. For example (Figure 2e), prostaglandin endoperoxide H synthase[37] (**7**) can be synthesized by using our strategy step-economically via intermediate **5** starting from 3-bromonitrobenzene (**4**). According to the literature, the synthesis of intermediate **5** requires three steps from **4**,[37] whereas our reaction conditions enable its synthesis in single step from **4**.

HAADF-STEM

To confirm the presence of copper (Cu) atom on the support, chemical mapping was conducted of the photocatalyst before and after the reaction by using energy dispersive X-ray spectroscopy (EDX) in low magnification scanning transmission electron microscopy (STEM) mode. As shown in Figure 3a, the EDX elemental maps indicated the presence of Cu (Figure S6), dispersed over the g-C_3N_4 support. The Cu-loading was quantified from various regions over the sample and was found to be 0.1–1 atom%. Furthermore, the high–resolution high-angle annular dark field scanning transmission electron microscopy (HAADF-STEM) image was used to distinguish the heavier metallic element, Cu, from the lighter support. Figure 3b shows high contrast for specific sites that are likely to agree with the presence of Cu as atomic sites randomly distributed over the C_3N_4 support. It is however to be noted that distinguishing single-atomic Cu sites from few-atomic Cu sites is difficult due to the difference in the contrast generated from the support (varying thickness). We have carefully chosen only thin edges of the supported catalyst where the contrast of Cu sites could be distinguished well from that of the supports. A similar analysis was repeated for the photocatalyst after the reaction. To our delight, the HAADF-STEM image (Figure 3c) again revealed a similar contrast, indicating no differences for Cu on the support. The corresponding EDX elemental maps (Figure 3d) furthermore confirmed the presence of Cu on the support. The EDX spectra used for quantification are shown in Supplementary Figure S6.

SS-NMR Study

To gain further insight into the local structure of the catalyst and to investigate any potential structural changes upon material doping with Cu^{2+} ions, solid–state magic angle spinning nuclear magnetic resonance (MAS NMR) was performed. The solid-state MAS NMR spectra of all NMR-active nuclei present in the material (^{1}H, ^{13}C, ^{15}N, and ^{19}F) are shown in Figure 3. The ^{1}H MAS NMR spectrum (Figure 3e) of Cu@f-gC_3N_4 showed two dominant signals at 8.6 and 3.9 ppm from —NH linkers and —NH_2 terminal

groups, respectively. The high intensity of the signal from —NH linkers compared to that of —NH_2 terminal groups indicated a high degree of polymerization. Figure 3f depicted two ^{13}C signals corresponding to the "edge" (C_e; 165 ppm) and the "internal" (C_i; 157 ppm) carbon sites, in accordance with the material structure. The higher intensity of the C_e signal than the C_i signal was expected since the distance between C_e and protons of the —NH and —NH_2 groups was shorter, allowing for more efficient cross-polarization in the CPMAS experiment. In the ^1H—^{15}N CPMAS spectrum (Figure 3g), nitrogen resonances from all four different types of nitrogen environments present in the material were observed. The signal at —187 and —223 ppm originated from the nitrogen atoms situated at the edge ($\mathbf{N_e}$) and inside ($\mathbf{N_i}$) of the monomer units, respectively. The number of N_e sites in relation to N_i was expected to be 6:1, but the signal integral at —187 ppm when compared —223 ppm was even higher than the factor of 6, since the distance of the N_i-type nitrogen atoms to the closest protons was substantially longer than in the case of N_e sites, which is in accordance with the material structure and corroborates signal assignment. The other two signals at —244 and —265 ppm corresponded to —NH linkers and —NH_2 terminal groups, respectively. Note that the signal of the latter group is overrepresented in the spectrum due to more efficient cross-polarization from the two protons involved. Considering that the ^1H MAS, ^{13}C CPMAS, and ^{15}N CPMAS spectra were comparable to the recently reported NMR study on the related polymeric carbon nitride,[38] it can be concluded that doping with Cu^{2+} ions did not significantly affect the overall structure and polymerization degree of the materials to any significant extent. However, in the ^{19}F MAS NMR spectrum shown in Figure 3h, a new signal appeared at —202 ppm in addition to the resonance signal at —105 ppm that was previously observed for the undoped polymeric carbon nitride. The ^{19}F chemical shift of —105 ppm indicated the presence of the =CF_2 moiety and consequently confirmed the successful incorporation of the fluorine atoms at one specific chemical site. To determine if the appearance of the signal at —202 ppm was due to the introduction of Cu^{2+} ions in the material, an additional ^{19}F MAS spectrum was recorded using a shorter relaxation delay (0.2 s, Figure 3h red trace). The spectrum showed that even using a shorter relaxation delay of 0.2 s, the intensity of the signal at —202 ppm was almost not affected, while the signal at —105 ppm was completely saturated and not observed in the spectrum under such detection conditions. This can be explained by paramagnetic relaxation enhancement for ^{19}F nuclei in close contact with paramagnetic Cu^{2+} ions. The additional signal with a shift of —202 ppm may have originated from an induced paramagnetic NMR shift due to unpaired electron(s) of the Cu^{2+} ions.[39]

XPS

The surface composition of Cu@f-gC_3N_4 was confirmed by X-ray photoelectron spectroscopy (XPS). Figure S5 (see in Supporting Information) exhibits the XPS peaks attributed to the g-C_3N_4 phase: (i) at 288.1 eV (sp^2-bonded C atoms in N—C=N) in the C 1 s region, as well as (ii) at 398.6 eV (sp^2-hybridized N atoms in C—N=C), 400.1 eV (bridging N atoms in N-$(C)_3$) and 401.2 eV (N atoms in amino groups) in the N 1 s region.[40,41] Additional confirmation of the presence of a properly developed g-C_3N_4 phase is the determined atomic ratio N/C = 1.4, which is very close to the expected one. The XPS Cu 2p spectrum shows the lack of distinct peaks, indicating a low content and high dispersion of Cu atoms on the surface.

XANES and EXAFS Experiments

The presence of isolated Cu single-atom active sites was further confirmed by analyzing the Cu@f-gC_3N_4 through XANES and EXAFS experiments, which show a clear fingerprint of the valence state and neighboring environment of the Cu atoms in the support matrix, respectively. Figure 4a compares the Cu K-edge XANES spectra of the photocatalyst with the reference spectra of Cu foil, CuO, CuO_2, and Cu(II)Pc, the near-edge feature of Cu@f-gC_3N_4 sample was in between of those of Cu_2O and CuO, indicating that the Cu species were partially positively charged ($Cu^{\delta+}$, $1< \delta< 2$).[42] Fourier-transformed *k*-weighted extended X-ray absorption fine structure (EXAFS) in R space was performed to elucidate the coordination environments of Cu atoms anchored on modified g-C_3N_4 (Figure 4b). For Cu@f-gC_3N_4, the major distinct scattering was observed at around 1.5 Å which corresponds to the first coordination shell of Cu-N/O and the minor peak at around 2.52 Å (not phase corrected), which seems to be at the same distance for $C_{32}H_{16}CuN_8$, which corresponds to the second coordination shell of Cu-C. The main peak at 1.50 Å and the higher shell peak at 2.52 Å coincide well with the Cu-N and Cu-C peaks for Cu(II)Pc ($C_{32}H_{16}CuN_8$), respectively.[43] Additionally, the peak at around 2.2 Å that is ascribed to Cu–Cu scattering cannot be observed in Cu@f-gC_3N_4. This evidence Cu exists as an isolated atom that is atomically dispersed on a modified g-C_3N_4 matrix through Cu—N—C bonding.[42,44,45] These findings are in perfect agreement with the HAADF-STEM results described above. Figure 4c,d shows the comparison between the FT of the experimental spectra (empty circles) and the best-fit simulations (colored lines) for the synthesized material. The coordination numbers, bond lengths, Debye–Waller factors (σ^2), and the energy shift parameter (ΔE_0) were refined. The best-fit parameters are summarized in Table S2 in Supporting Information. The first shell best-fit results show that each Cu atom is coordinated with 2 N/O atoms on average.[46]

EPR Spectroscopy

Further evidence about the existence of Cu single atom sites as well as their coordination to N atoms was obtained from EPR spectroscopy. The EPR spectrum of the Cu@f-gC_3N_4 catalyst (Figure S7, Supporting Information) exhibited an axial signal at $g_\perp = 2.06$ and $g_\parallel = 2.173$ with well-resolved hyperfine structure (HFS) $A_\parallel = 198$ G due to the coupling of the single electron spin of Cu^{II} (d^9, $S = 1/2$) with the nuclear

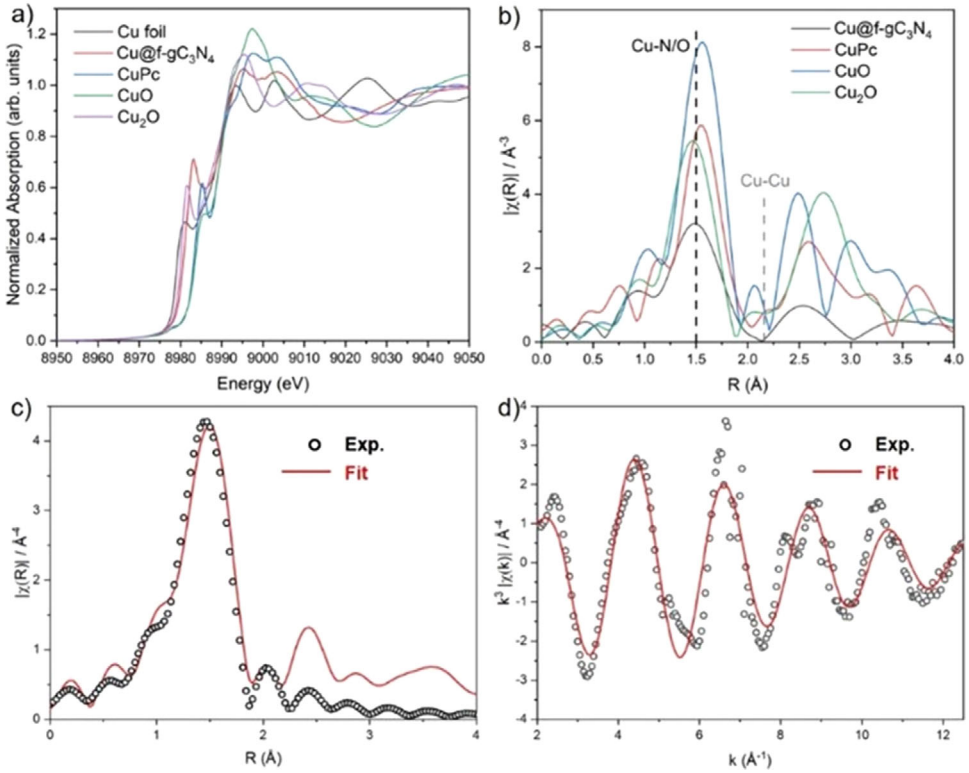

Figure 4. Normalized Cu K-edge XANES spectra a) and Fourier transform of the k^3-weighted EXAFS b) for Cu@f-gC_3N_4 photocatalyst, Cu foil, CuO, CuO_2, and Cu (II)Pc ($C_{32}H_{16}CuN_8$). Data (empty circles) and fits (red lines) of the magnitude of the FT signal c) and the k^3-weighted EXAFS signals in *k*-space d).

spin of Cu ($I = 3/2$), indicating the presence of isolated Cu^{II} ions. Moreover, the perpendicular component of the g tensor showed a 9-line super-hyperfine structure (SHFS) as evident from the corresponding 1st derivative of the EPR spectrum Figure S7b, Supporting Information). This splitting is on the order of 2nI + 1 ($n = 4$; $I = 1$) and with a coupling constant of 16 G, indicating a coordination of four nitrogen atoms to Cu sites (^{14}N, $I = 1$).

The anticipated course of the direct C(sp^2)─H trifluoromethylation of arenes with Togni-I reagent, utilizing Cu@f-gC_3N_4 photocatalyst was envisioned to follow a radical mechanism. To probe this radical pathway, a radical quenching experiment (Figure S2.8A, Supporting Information) was conducted by subjecting nitrobenzene (**1a**) to Togni-I (**2a**) reagent under the optimized reaction conditions in the presence of (2,2,6,6-tetramethylpiperidine-1-yl)oxyl (TEMPO, 3.0 equiv). The introduction of TEMPO into the reaction mixture resulted in a pronounced inhibition of the trifluoromethylation process, ultimately preventing the detection of the trifluoromethylated product. Similarly, the replacement of TEMPO by butylated hydroxytoluene (BHT, 2.0 equiv) as a spin trap yielded no observable product. Furthermore, when the model reaction was conducted with suitable ligands (4-bromobenzenethiol and butan-1-amine), which can coordinate with the active site of Cu in the photocatalyst, the desired product 3a was achieved in 19% (*p/m* = 2:1) and 26% (*p/m* = 2:1) yields, respectively (Figure S2.8B, Supporting Information). This experimental validation showcased the significance of the Cu-active site in the photocatalyst's efficacy. Additionally, to ascertain whether the rate-determining step was involved with the breaking of the C─H bond, a kinetic isotope effect (KIE) analysis was undertaken (Figure S2.8C, Supporting Information) and strongly implied that this reaction does not involve Friedel–Crafts type reaction mechanism ($K_H/K_D = 1.85$).

Moreover, to elucidate the metal-substrate interaction in a η2 fashion, wherein the Cu(I) atom forms a direct connection with the arene substrates through an aromatic Cortho-Cmeta bond of the ring,[47,48] we employed the para-blocked substrate (product **3a** and **3n**) under the optimized reaction conditions (Figure S2.8D, Supporting Information). Our observations revealed the absence of any aromatic C─H bond functionalized product, substantiating the hypothesis of η2-bonding between the Cu-metal and the ortho/meta carbon of the aromatic substrate. Additionally, XANES/EXAFS spectra further confirmed the isolated Cu sites with a coordination environment favoring η^2-binding. These analyses explicitly link the catalyst's atomic structure to the steric-driven regioselectivity.We have investigated, by density functional theory calculations (DFT), the preferential substitution of the para- position considering a reduced model of the Cu@f-gC3N4 photocatalyst made of two melamine subunits, a fluorinated ligand, and a single coordinated Cu atom. Previous studies and electron paramagnetic resonance (EPR) characterizations have indicated that this model accurately represents the heightened catalytic activity of the material.[49]

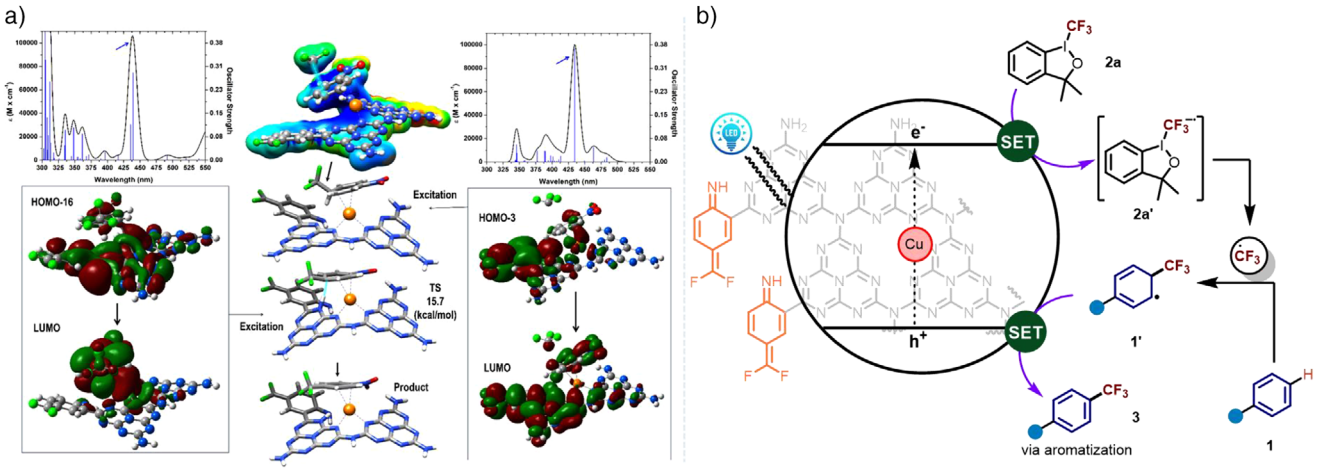

Figure 5. a) Molecular electrostatic potential map (au units) of the catalyst–nitrobenzene–CF_3 complex projected onto the corresponding molecular electron densities calculated at the B3LYP/6–31G(d,p)+LANL08 level in acetonitrile solution. Red regions represent negative electrostatic potential (highest electron density -0.06), whereas blue regions represent positive potentials (lowest electron density +0.06). The graphical representations were generated by mapping the ESP onto a molecular surface corresponding to an isodensity contour at 0.1 e au^{-3} using UCSF Chimera.[50] Predicted UV–vis spectra of the catalyst–nitrobenzene–CF_3 complex (top right) and intermediate catalyst-nitrobenzene catalyst–nitrobenzene–CF_3.geometry (top left). The orbitals involved in the dominant transitions are displayed below the absorption plots. The mechanism to get the final product is shown in the middle. Color codes: Cu orange, N blue, C grey, O red, F green, and H white. b) Proposed mechanism.

This enhancement primarily arises from the entrapment of the Cu atom between two pyridinic nitrogen of the f-gC_3N_4 rings, the presence of the adjacent ligand (Figure S8, see in Supporting Information), which determines an optimal d-band position for the catalyst, the system's absorption in the blue region of the spectrum, and the direct adsorption of the reactant onto the metal center through a C─C bond on the ring. Subsequently, the photocatalyst activates the para-C─H bond of the arene complex due to the adopted preferential binding mode of the benzene ring. This observation aligns well with existing literature.[47,48] All the calculations were first carried out on the nitrobenzene reactant to reproduce all the steps of the mechanism leading to the final products. The optimized configuration of the catalyst-reactant complex resulted in an almost stacked geometry of the nitrobenzene and melamine unit, with the nitrobenzene molecule directly connected to the Cu(I) atom through an aromatic Cortho─Cmeta bond of the ring, which slightly elongated from 1.39 to 1.41 Å.[47] This proposed η^2-benzene bonding was also obtained in all the substituted species examined in this work and confirmed by previous X-ray crystallography studies for other systems.[48] The coordination of Cu to the ring nitrogen was found at similar, slightly shorter distances of about 2.06 Å. Instead, the preferential location of the ─NO2 group (and the other substituents of the considered adsorbed species) was in the region of the photocatalyst's ligand but inclined toward the opposite direction to minimize unfavorable interactions (similar MEP zones).

The NBO analysis helped to interpret the system's charge distribution to disclose the arene ring's activation mechanism. Before the adsorption of nitrobenzene, the Cu-cation was trapped between the nitrogen of two opposite triazine rings had a charge of approximately +0.85. Still, after the adsorption of the molecule, Cu showed a reduced net charge of roughly +0.74, whereas the LIG-f-gC_3N_4 system (photocatalyst) and nitrobenzene had −0.40 and −0.34 charges, respectively. This suggested that the electron density flowed from the photocatalyst (mainly the ligand – Figure S8 red regions, see in Supporting Information) to the adsorbed nitrobenzene-Cu orbitals, and the *para*-C─H bond (with a total charge of +0.11 compared to the −0.04 charge of the meta positions) was found more prone to accept the vacant radical anion CF_3 moiety placed nearby (Figure 5a). Besides rationalizing a more probable *para* substitution by looking at the local NBO charges, we resorted to the visualization of the molecular electrostatic potential maps projected onto the corresponding one-electron densities at the level of the theory mentioned above to confirm the adsorption scenario. As shown in Figure S8 (see in Supporting Information), the MEP of nitrobenzene is positive everywhere above the aryl plane and negative in the regions of the oxygen/nitrogen lone pairs (and fluorine), indicating that both the catalyst ligand and the ─NO_2 moiety are relatively strong inductive electron-withdrawing groups. The MEPs of the complexes, with and without (Figure 5a) the ─CF_3 group placed on top of nitrobenzene, show a redistribution of the charges (thus slightly different MEP areas) and reveal that the *para*-C─H site was less hindered and more complementary to the approaching species.

Moving to the calculations of the UV–vis spectra of the optimized structures, we also found that the catalyst/reactant complexes had intense absorption bands centered in the 425–450 nm range, which practically corresponded to the LED emission region. After optimizing the three-component geometry, we obtained a stable intermediate structure (where the CF_3 carbon was on top of the *para* ring carbon at about 3.3 Å separation – Figure 5a **top configuration**). Then, we calculated the UV–vis spectrum (Figure 5a), which revealed a dominant transition at about 434 nm (HOMO-3 LUMO) responsible for the formation of the F_3C─C

bond, as evidenced by the involved orbitals represented in Figure 5a. Again, we optimized this intermediate complex, obtaining a bounded structure, and then predicted its UV absorption spectrum (Figure 5 **top left spectrum**). This showed a dominant peak corresponding to a transition from the catalyst to the adsorbed complex (HOMO-16 to LUMO – Figure 5a **left orbitals**). The excited state optimization produced the geometry corresponding to the transition state shown in Figure 5a (structure in the middle), where the *para*-*C*—H was halfway from C to N. Then, the transfer to the closer nitrogen on the melamine unit was completed in the final optimized product (Figure 5a **bottom structure**). The estimated energy barrier $\Delta E^{\ddagger}$ was about 16 kcal mol^{-1}.

After demonstrating that LED light induced the adsorption of —CF_3 on the *para* site, we estimated the energy of the intermediate complexes (obtained after the first excitation) of other species where the NO_2 moiety was replaced with the —CF_3, —CN, and —OCH_3 groups (Table S3, Supporting Information). In these optimized complexes, the arenes adopted similar binding modes and were all prone to accept the —CF_3 moiety in the *para* position (Table S3, Supporting Information). An estimate of the reactant and transition structures (where the ring H was transferred to the catalyst) energies also confirmed in these cases the *para* preference (Table S3, Supporting Information).

Drawing upon the outcomes of preliminary optimization trials (Table 1), control experiments (Figure S2.8, Supporting Information), DFT calculation and pertinent references in the literature, we proposed the following mechanistic pathway for the photocatalytic trifluoromethylation process (Figure 5b).

Initiated by blue LED irradiation, the Cu@f-gC_3N_4 photocatalyst underwent activation, generating positive holes at the valence band and an excess of electrons at the conduction band on its surface. The trifluoromethyl radical (•CF_3) species emerged through a single electron transfer (SET) from the catalyst's conduction band (E_{CB} = −1.40 V vs. SCE) to the trifluoromethylating agent **2a** ($E_{1/2}$ = −0.18 to −1.09 V vs. SCE).[30,51] Following this, the trifluoromethyl radical interacted with the arene substrate, resulting in a CF_3-inserted arene radical intermediate 1′. This C-radical intermediate underwent oxidation at the valence band, forming a carbocation intermediate. Subsequent deprotonation facilitated the regeneration of the aromatic system, ultimately yielding the desired trifluoromethylated product **3**. We further calculated the quantum yield of this process to assess whether the reaction followed a radical chain mechanism (see the ESI for details), and the low quantum yield (Φ = 1.01) indicated that a radical chain process was unlikely to be involved. In a nutshell, from the mechanistic experiments and DFT calculation it is conclusive that regioselectivity is not governed by the electronic nature of substituents. Instead, steric control via the η^2-bonding interaction between the Cu catalyst and the aromatic ring is the dominant factor.

The theoretical viability of this reaction pathway is supported by DFT calculations which also suggest a possible mechanism for alternative regioselective product formation involving the preferential insertion of the incoming radical in *para* position. This analysis revealed that the preferential position (the *para*-position) for aromatic functionalization, is less hindered and complementarity to the approaching radical species.

Conclusion

In summary, we have outlined and rationalized via advanced experimental characterizations and modeling an efficient strategy for the *para*-functionalization of arenes by using an atomically dispersed Cu photocatalyst which does not require the presence of a directing group. This study is articulated into two key segments: first, the formulation and synthesis of a Cu-based catalyst with atomic dispersion of coordinated Cu sites on an aryl-amino-substituted graphite carbon nitride; second, the application of this photocatalyst for accomplishing an unprecedented *para*-selective C—H trifluoromethylations of electron-poor arenes.

Acknowledgements

S.D. thanks the UBT start-up funding for the financial support. S.P. thanks DTU for the postdoctoral funding. J.H. thanks UBT for PhD funding. P.R. and Y.Q. thank CSC scholarship no 2020026870012 for their PhD funding. J.S.A acknowledges financial support from MCIN (Project PID2022-142960OB-C21) and Conselleria de Innovación, Universidades, Cienciay Sociedad Digital, Generalitat Valenciana (Project CIPROM/2021/022). J.S.A. acknowledges beamtime allocated at B18 endstation (Diamond, UK), rapid access proposal SP32609-1. A.R. and P.K. thank Smart Growth Operational Programme (contract no. POIR.04.02.00–00-D001/20) and Strategic Programme Excellence Initiative at Jagiellonian University for funds for the purchase and maintenance of the XPS measurement system.

Open access funding enabled and organized by Projekt DEAL.

Conflict of Interests

The authors declare no conflict of interest.

Data Availability Statement

The data that support the findings of this study are available in the Supporting Information of this article.

Keywords: Atomically dispersed photocatalyst (AD-PC) · Electron-poor-arene · Orthogonal *para*-selectivity · Photocatalysis · Trifluoromethylation

[1] L. Guillemard, N. Kaplaneris, L. Ackermann, M. J. Johansson, *Nat. Rev. Chem.* **2021**, *5*, 522–545.
[2] X.-S. Xue, P. Ji, B. Zhou, J.-P. Cheng, *Chem. Rev.* **2017**, *117*, 8622–8648.

[3] C. Friedel, J. Crafts, *J. Chem. Soc* **1877**, *32*, 725–791.
[4] Y. Goto, M. Sano, Y. Sumida, H. Ohmiya, *Nat. Synth.* **2023**, *2*, 1037–1045.
[5] B. Ramadoss, Y. Jin, S. Asako, L. Ilies, *Science* **2022**, *375*, 658–663.
[6] L.-Y. Liu, J. X. Qiao, K.-S. Yeung, W. R. Ewing, J.-Q. Yu, *J. Am. Chem. Soc.* **2019**, *141*, 14870–14877.
[7] D.-H. Wang, T.-S. Mei, J.-Q. Yu, *J. Am. Chem. Soc.* **2008**, *130*, 17676–17677.
[8] U. Dutta, S. Porey, S. Pimparkar, A. Mandal, J. Grover, A. Koodan, D. Maiti, *Angew. Chem. Int. Ed.* **2020**, *59*, 20831–20836.
[9] C. Cheng, J. F. Hartwig, *Science* **2014**, *343*, 853–857.
[10] Y. Saito, Y. Segawa, K. Itami, *J. Am. Chem. Soc.* **2015**, *137*, 5193–5198.
[11] B. E. Haines, Y. Saito, Y. Segawa, K. Itami, D. G. Musaev, *ACS Catal.* **2016**, *6*, 7536–7546.
[12] G. B. Boursalian, W. S. Ham, A. R. Mazzotti, T. Ritter, *Nat. Chem.* **2016**, *8*, 810–815.
[13] F. Berger, M. B. Plutschack, J. Riegger, W. Yu, S. Speicher, M. Ho, N. Frank, T. Ritter, *Nature* **2019**, *567*, 223–228.
[14] X.-Y. Chen, Y.-N. Li, Y. Wu, J. Bai, Y. Guo, P. Wang, *J. Am. Chem. Soc.* **2023**, *145*, 10431–10440.
[15] G. Meng, J.-L. Yan, N. Chekshin, D. A. Strassfeld, J.-Q. Yu, *ACS Catal.* **2024**, *14*, 12806–12813.
[16] S. Gisbertz, B. Pieber, *ChemPhotoChem* **2020**, *4*, 456–475.
[17] V. B. Saptal, V. Ruta, M. A. Bajada, G. Vilé, *Angew. Chem. Int. Ed.* **2023**, *62*, e202219306.
[18] M. E. Hoque, R. Bisht, C. Haldar, B. Chattopadhyay, *J. Am. Chem. Soc.* **2017**, *139*, 7745–7748.
[19] S. Okumura, S. Tang, T. Saito, K. Semba, S. Sakaki, Y. Nakao, *J. Am. Chem. Soc.* **2016**, *138*, 14699–14704.
[20] M. Li, M. Shang, H. Xu, X. Wang, H.-X. Dai, J.-Q. Yu, *Org. Lett.* **2019**, *21*, 540–544.
[21] F. O'Hara, D. G. Blackmond, P. S. Baran, *J. Am. Chem. Soc.* **2013**, *135*, 12122–12134.
[22] C. Copéret, A. Comas-Vives, M. P. Conley, D. P. Estes, A. Fedorov, V. Mougel, H. Nagae, F. Núñez-Zarur, P. A. Zhizhko, *Chem. Rev.* **2016**, *116*, 323–421.
[23] C. Vogt, B. M. Weckhuysen, *Nat. Rev. Chem.* **2022**, *6*, 89–111.
[24] M. A. Bajada, G. Di Liberto, S. Tosoni, V. Ruta, L. Mino, N. Allasia, A. Sivo, G. Pacchioni, G. Vilé, *Nat. Syn.* **2023**, *2*, 1092–1103.
[25] X. Cui, W. Li, P. Ryabchuk, K. Junge, M. Beller, *Nat. Cat.* **2018**, *1*, 385–397.
[26] C. Gao, J. Low, R. Long, T. Kong, J. Zhu, Y. Xiong, *Chem. Rev.* **2020**, *120*, 12175–12216.
[27] N. Fechler, N. P. Zussblatt, R. Rothe, R. Schlögl, M.-G. Willinger, B. F. Chmelka, M. Antonietti, *Adv. Mater.* **2016**, *28*, 1328.
[28] J. B. Zimmerman, P. T. Anastas, H. C. Erythropel, W. Leitner, *Science* **2020**, *367*, 397–400.
[29] K. Müller, C. Faeh, F.ranço. Diederich, *Science* **2007**, *317*, 1881–1886.
[30] D. A. Nagib, D. W. C. MacMillan, *Nature* **2011**, *480*, 224–228.
[31] E. J. Cho, T. D. Senecal, T. Kinzel, Y. Zhang, D. A. Watson, S. L. Buchwald, *Science* **2010**, *328*, 1679–1681.
[32] C. M. Kisukuri, V. A. Fernandes, J. A. C. Delgado, A. P. Häring, M. W. Paixão, S. R. Waldvogel, *Chem. Rec.* **2021**, *21*, 2502–2525.
[33] Y. Zhang, T. Zhang, S. Das, *Chem* **2022**, *8*, 3175–3201.
[34] C. J. Wenthur, M. R. Bennett, C. W. Lindsley, *ACS Chem. Neurosci.* **2014**, *5*, 14–23.
[35] X. Wu, J. Xu, F. Dong, X. Liu, Y. Zheng, *J. Hazard. Mater.* **2014**, *273*, 155–164.
[36] A. Kamel, S. Al-Dosary, S. Ibrahim, M. Asif Ahmed, *Food Chem.* **2007**, *100*, 1590–1593.
[37] Arylpyridazinones as selective cyclooxygenase-2 inhibitors, *Exp. Opin. Ther. Patents* **1999**, *9*, 1733–1738, https://doi.org/10.1517/13543776.9.12.1733.
[38] T. Zhang, W. Schilling, S. U. Khan, H. Y. V. Ching, C. Lu, J. Chen, A. Jaworski, G. Barcaro, S. Monti, K. De Wael, A. Slabon, S. Das, *ACS Catal.* **2021**, *11*, 14087–14101.
[39] A. Jaworski, N. Hedin, *Phys. Chem. Chem. Phys.* **2022**, *24*, 15230–15244.
[40] Y. Huang, B. Chen, J. Duan, F. Yang, T. Wang, Z. Wang, W. Yang, C. Hu, W. Luo, Y. Huang, *Angew. Chem. Int. Ed.* **2020**, *59*, 3699–3704.
[41] F. Dong, Z. Zhao, T. Xiong, Z. Ni, W. Zhang, Y. Sun, W.-K. Ho, *ACS Appl. Mater. Interfaces* **2013**, *5*, 11392–11401.
[42] Y. Chen, H. Zou, B. Yan, X. Wu, W. Cao, Y. Qian, L. Zheng, G. Yang, *Adv. Sci. (Weinh)* **2022**, *9*, e2103977.
[43] H. Fei, J. Dong, C. Wan, Z. Zhao, X. Xu, Z. Lin, Y. Wang, H. Liu, K. Zang, J. Luo, S. Zhao, W. Hu, W. Yan, I. Shakir, Y. Huang, X. Duan, *Adv. Mater.* **2018**, *30*, 1802146.
[44] F. Huang, Y. Deng, Y. Chen, X. Cai, M. Peng, Z. Jia, J. Xie, D. Xiao, X. Wen, N. Wang, Z. Jiang, H. Liu, D. Ma, *Nat. Commun.* **2019**, *10*, 4431.
[45] Z. Jiang, W. Sun, H. Shang, W. Chen, T. Sun, H. Li, J. Dong, J. Zhou, Z. Li, Y. Wang, R. Cao, R. Sarangi, Z. Yang, D. Wang, J. Zhang, Y. Li, *Energy Environ. Sci.* **2019**, *12*, 3508–3514.
[46] N. S. Devi, L. J. Singh, S. P. Devi, R. K. B. Singh, R. K. H. Singh, B. Rajeswari, R. M. Kadam, *J. Coord. Chem.* **2011**, *64*, 4108–4121.
[47] T. Archipov, S. Santra, A. B. Ene, H. Stoll, G. Rauhut, E. Roduner, *J. Phys. Chem.* **2009**, *113*, 4107–4116;
[48] C. N. Iverson, R. J. Lachicotte, C. Müller, W. D. Jones, *Organometallics* **2002**, *21*, 5320–5333.
[49] P. Ren, T. Zhang, N. Jain, H. Y. V. Ching, A. Jaworski, G. Barcaro, S. Monti, J. Silvestre-Albero, V. Celorrio, L. Chouhan, A. Rokicińska, E. Debroye, P. Kuśtrowski, S. van Doorslaer, S. van Aert, S. Bals, S. Das, *J. Am. Chem. Soc.* **2023**, *145*, 16584–16596.
[50] E. F. Pettersen, T. D. Goddard, C. C. Huang, G. S. Couch, D. M. Greenblatt, E. C. Meng, T. E. Ferrin, *J. Comput. Chem.* **2004**, *25*, 1605–1612.
[51] J. Charpentier, N. Früh, A. Togni, *Chem. Rev.* **2015**, *115*, 650–682.

Manuscript received: April 16, 2025
Revised manuscript received: June 09, 2025
Accepted manuscript online: June 09, 2025
Version of record online: July 01, 2025